Electrochemical performance of a portable asymmetric supercapacitor device based on cinnamon-like La$_2$Te$_3$ prepared by a chemical synthesis route

Swati J. Patil, Bebi H. Patil, Ravindra N. Bulakhe and Chandrakant D. Lokhande*

A cinnamon-like La$_2$Te$_3$ nanostructure has been prepared by a simple chemical bath deposition (CBD) route. Field emission-scanning electron microscopy (FE-SEM), X-ray diffraction (XRD) and Fourier transform infrared (FTIR) spectroscopy techniques have been used to characterize the morphological and structural properties of the La$_2$Te$_3$ thin films. The prepared La$_2$Te$_3$ thin film electrodes are applied in a supercapacitor, in which they exhibited a high specific capacitance value of 469 F g^{-1} at a scan rate of 2 mV s^{-1} with an excellent cycling performance up to 1000 cycles. Even at a specific power of 2.5 kW kg^{-1}, the La$_2$Te$_3$ electrode possessed a specific energy of ~126 Wh kg^{-1}. At a relatively high discharge current density of 4 mA cm^{-2}, the specific capacitance was still maintained at 220 F g^{-1}. Furthermore, portable La$_2$Te$_3$ asymmetric supercapacitor devices have been fabricated using an aqueous 1 M KOH electrolyte with good specific energy and specific power. Such an impressive portable asymmetric supercapacitor is a promising candidate for applications in high-performance energy storage systems.

Introduction

The rising prices of fossil fuels, in addition to their rapid depletion and the pollution caused by their combustion, has led to the extensive search for clean renewable energy sources and energy storage devices. Batteries, fuel cells and supercapacitors are electrical energy storage devices that store energy in the form of a charge. Among these, supercapacitors, which are also known as electrochemical capacitors (ECs) or ultracapacitors, are quite attractive because they can provide a power density greater than batteries or fuel cells and much higher energy density than conventional capacitors. A supercapacitor can be generally classified as either an electrical double-layer capacitor (EDLC) or a pseudocapacitor.[1] The EDLCs store energy through the accumulation of charges at the interface of an electrode and electrolyte. In EDLCs, the energy storage mechanism allows for a long-term stability and fast charge–discharge, these include carbon-based materials.[2] A pseudocapacitor is the second type of supercapacitor and it can store energy through redox or faradaic reactions between the electrode material and electrolyte. Generally, metal oxides, such as Mn$_3$O$_4$,[3] NiO[4] and conducting polymers,[5] are included under this type. There has been a recent trend of using metal sulphides as supercapacitor electrodes due to their wide potential window, good capacitance

retention and better charge–discharge performance.[6] Of these, the rare earth sulphides showed a good contribution in electrochemical activity.[7,8] Similarly, metal tellurides are of interest in solid-state chemistry and materials science because of their physical properties and rich structural chemistry. These semiconductors are primarily used as alloys to improve the thermal, optical, and electrical properties of devices in various fields. Graf *et al.*[9] demonstrated that polytellurides, in solid-state material applications, such as rechargeable batteries, are in the form of polychalcogenides. Among the rare earth tellurides, lanthanum telluride is known to show thermoelectric properties due to its high thermal stability.[10]

Several methods based on physical and chemical approaches have been developed for the synthesis of nanostructure particles in the form of thin films with controlled sizes and shapes.[11] Good quality thin films of La$_2$Te$_3$ with suitable thermoelectric properties have been produced by spray pyrolysis deposition.[12] Pereira *et al.*[13] described the preparation of lanthanide tellurites in an aqueous medium of hydrogen and neutral telluride of lanthanum. Ramsey *et al.*[14] summarized the thermoelectric properties of a polycrystalline lanthanum telluride. Samal *et al.*[15] synthesized La$_2$Te$_3$ nanowires in the solution phase. However, these deposition methods have some drawbacks concerning the mass production of relatively thick layers (around 100 micrometers). To the best of our knowledge, there are no reports on the electrochemical supercapacitive performance of an La$_2$Te$_3$ electrode and its use in the fabrication of a supercapacitor device.

Thin Film Physics Laboratory, Department of Physics, Shivaji University, Kolhapur – 416 004, India. E-mail: l_chandrakant@yahoo.com; Fax: +91 231 26092333; Tel: +91 231 2609223

Herein, lanthanum telluride (La_2Te_3) thin films were synthesized by a simple chemical bath deposition (CBD) route. The structural, morphological and wettability properties were studied as they play an important role in determining the specific capacitance of the La_2Te_3 electrode. The supercapacitive properties of the La_2Te_3 electrode were studied in an aqueous KOH electrolyte, which offers the advantages of being cost effective, non-flammable, and easy to handle as well as ionic conductivity. A portable asymmetric supercapacitor device based on the La_2Te_3 electrode was fabricated and its supercapacitive performance was tested.

Experimental details

Lanthanum telluride (La_2Te_3) thin films were synthesized from an aqueous bath by a simple, cost effective, chemical bath deposition (CBD) route. In the typical synthesis of the La_2Te_3 thin films, AR grade hydrochloric acid (HCl, 35%), nitric acid (HNO$_3$, 65%), ethylenediaminetetraacetic acid (EDTA, $C_{10}H_{16}N_2O_8$), lanthanum oxide (La_2O_3), tellurium powder were used without further purification. In the first step, a solution containing Te^{+2} ions was prepared. Tellurium powder (1 g) was partially dissolved in 10 mL aqueous solution, consisting of concentrated HCl and HNO$_3$ in the volumetric ratio of 1 : 1. The 10 mL prepared acidic solution was mixed in 200 mL of doubly distilled water (DDW) at 80 °C for 15 min using a magnetic stirrer. In the second step, the lanthanum ion (La^{+3}) solution was prepared by dissolving 0.1 M of lanthanum oxide (La_2O_3) in 40 mL diluted 1 M HCl to form lanthanum chloride ($LaCl_3$) in the bath. Equimolar solutions of lanthanum and telluride ions were mixed in a 40 : 60 mL volumetric ratio to prepare the final 100 mL solution. The reaction mixture was stirred constantly for 10 min at room temperature (273 K). Finally, well-cleaned stainless steel substrates were dipped in the reaction mixture for 30 min to obtain silver-blackish colored La_2Te_3 films on the stainless steel substrates. Furthermore, the La_2Te_3 films were air-annealed at 473 K in a tube furnace for 1 h to improve their crystallinity.

Characterization techniques

Structural characterization

The phase composition and structural characterization of the La_2Te_3 thin films were obtained using an X-ray diffractometer (XRD, Bruker AXS D8 Advance Model) operating in the diffraction mode with CuKα radiation ($\lambda = 0.154$ nm) in the range of 10–80°. The Fourier transform infrared (FTIR, Perkin Elmer spectrum 400 spectrophotometer) data was recorded with a scan range of 650–3000 cm^{-1}. The surface morphology of the La_2Te_3 thin films was examined by a field emission-scanning electron microscope (FE-SEM, SU8000, Hitachi). The water contact angle of the La_2Te_3 film surface was measured using a digital Goniometer (Rame-Hart NRL CA) fabricated with an automatic dispensing needle in an ambient environment.
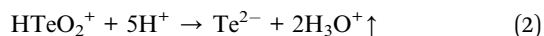
Electrochemical measurements

The cyclic voltammetry (CV) and galvanostatic charge–discharge (GCD) studies were carried out using an automatic battery cycler (WBCS3000). Electrochemical impedance spectroscopy (EIS) was used to characterize the interface quality between the electrode and electrolyte, by an electrochemical workstation (Model Zive SP5). All of the electrochemical characterizations were performed in a standard three-electrode cell configuration with a platinum wire as a counter electrode, saturated calomel electrode (SCE) as a reference electrode and the La_2Te_3 thin film as a working electrode. The electrochemical performance of the La_2Te_3 electrode was measured in a 1 M KOH electrolyte in −0.3 to −1.3 V potential windows.

Results and discussion

Film formation and reaction mechanism

The combination of an electropositive lanthanum (La^{3+}) metal cation and a polarizable telluride (Te^{2-}) anion ligand makes reactive La–Te bonds. For the formation of the La_2Te_3 thin film in the reaction bath, the following reactions are assumed.

When the Te powder is dissolved in an equimolar concentration of HCl and HNO$_3$, the $HTeO_2^+$ and H^+ are separated in reaction bath by the vaporization of NOCl,

$$HCl + HNO_3 + Te_{(s)} \rightarrow HTeO_2^+ + H^+ + NOCl\uparrow \qquad (1)$$

$$HTeO_2^+ + 5H^+ \rightarrow Te^{2-} + 2H_3O^+\uparrow \qquad (2)$$

The solution of $LaCl_3$ is formed, when La_2O_3 is dissolved in diluted HCl.

$$La_2O_3 + 6HCl \rightarrow 2LaCl_3 + 3H_2O \qquad (3)$$
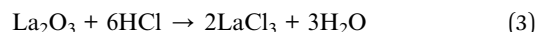
Finally, the La complex is formed using EDTA ($C_{10}H_{16}N_2O_8$) as a complexing agent as follows:

$$2LaCl_3 + 2(C_{10}H_{16}N_2O_8) \rightarrow 2[La(C_{10}H_{16}N_2O_8)]^{+3} + 3Cl_2 \quad (4)$$
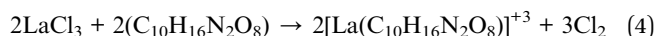
The complex of La^{+3}, [La ($C_{10}H_{16}N_2O_8$)]$^{+3}$ reacts with Te^{-2} to form La_2Te_3 as follows:

$$2[La(C_{10}H_{16}N_2O_8)]^{+3} + 3Te^{-2} \rightarrow La_2Te_3 + 2C_{10}H_{16}N_2O_8 \quad (5)$$
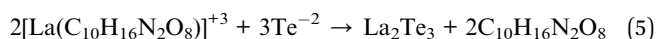
In the composition of the La_2Te_3 prepared, each La donates three electrons forming La^{+3}, and Te utilizes two of these to complete the valance to become Te^{-2}.[16] Finally, uniform and adherent La_2Te_3 thin films are coated on the substrate.

Thickness measurement study

The thickness of the La_2Te_3 film was calculated by a gravimetric method. The typical working electrode was 0.301 mg in weight with a surface area of 1 cm^2 and its thickness was 456 nm, which was calculated by using the formula:

$$t = \frac{m_2 - m_1}{\rho \times A} \qquad (6)$$

where m_1 and m_2 are the masses of electrode material before and after deposition, ρ (6.6 g cm^3) is the density of electrode material,[12] A (cm^2) is the active area of the electrode material deposited on the steel substrate and t (nm) is the thickness of thin film electrode.

X-ray diffraction (XRD) study

Fig. 1(A) shows the XRD pattern of a La$_2$Te$_3$ thin film on a stainless steel substrate. The main diffraction peak indexed at 27.34° for the (220) plane is matched with the standard JCPDS card no. 019 0662 for the La$_2$Te$_3$ cubic phase. Other planes such as the (211), (220), (321), (541), and (642) also corresponds to the cubic phase of the La$_2$Te$_3$ material. The observed additional peak at 40.60° along the (110) plane is best matched with the (JCPDS 002-0511) Te material. Skhouni *et al.*[17] observed the separate Te peak in an electrodeposited ZnTe thin film. The crystallite size of the La$_2$Te$_3$ thin film material was estimated using Scherer's equation as follows:

$$D = \frac{0.9\lambda}{\beta \cos \theta} \qquad (7)$$

where D is the crystallite size, λ is the wavelength (0.154 nm), β is the full width at half maxima and θ is the diffraction angle. The estimated values of the crystallite size for all planes are summarized in Table 1. The crystallite size was found to be 67.9 nm for the plane (220).

Fourier transform infrared (FTIR) study

Fourier transform infrared spectroscopy (FTIR) is another powerful technique, which was used to analyze the chemical bands present in the synthesized film material. The FTIR spectrum of the La$_2$Te$_3$ thin film is shown in Fig. 1(B). The assignment of the various bands is given in Table 2. The band at 1681 cm^{-1} is assigned to the La$_2$Te$_3$ material formation, while the peaks at around 1012 and 1670 cm^{-1} are La(O–H) and La$_2$O$_3$, respectively, in the spectrum, which can be attributed to the La–O stretching vibrations.[18] The band displayed at 1090 cm^{-1} is assigned to the symmetric stretching vibration of (–C–O).[19] The band observed at 1486 cm^{-1} is due to the bending of the δ (C–H) of the CH$_3$ group.[20] The peak at 1578 cm^{-1} is due to the υ (C–C) aromatic ring vibration.[21] The peak at 1294 cm^{-1} is due to the C–N stretching vibrations.[22] The above organic bands occurred in the La$_2$Te$_3$ pattern due to residual EDTA, which was added as a complexing agent during deposition. Hence, the IR measurement establishes the structure of the La$_2$Te$_3$ formation.

Field emission-scanning electron microscopy (FE-SEM) study

The surface morphological architecture of the La$_2$Te$_3$ film was studied by using field-emission scanning electron microscopy (FE-SEM). Fig. 2(A and B) show the FE-SEM micrographs of the La$_2$Te$_3$ thin film at magnifications of 5000× and 15 000×, respectively. The FE-SEM reveals the interconnected network of La$_2$Te$_3$ with a cinnamon-like morphology. Fig. 2(B) shows cinnamon-like surface with an average thickness of about one thousand nanometers (~1 μm) and lengths of up to ten micrometers (~10 μm). The cinnamon-like rough surface
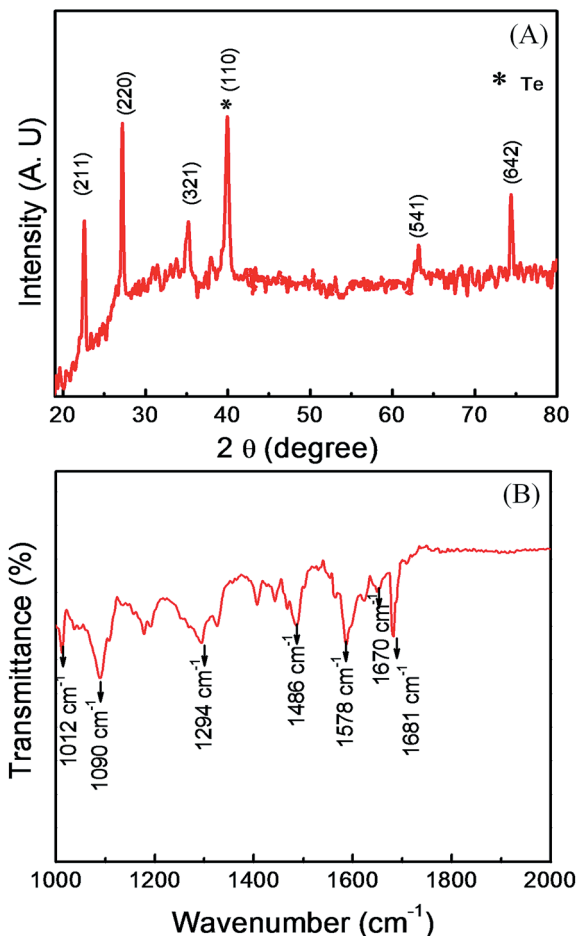

Fig. 1 (A) XRD pattern and (B) FTIR spectrum of the cinnamon-like La$_2$Te$_3$ thin film on a stainless steel substrate.

offered sufficient reservoirs for an electrolyte, which is desirable for the good performance of a supercapacitor electrode. The top inset in Fig. 2(B) shows the actual image of cinnamon. As seen in Fig. 2(B), the coarse grain structure with intergranular spacings may be due to the presence of Te, which is also observed in the XRD pattern.[17]

Contact angle study. The wettability study of the La$_2$Te$_3$ thin film was carried out by a water droplet on the La$_2$Te$_3$ film surface. The image of the water contact angle of the La$_2$Te$_3$ film surface is shown in Fig. 3. The measured water contact angle of 20° suggests that the La$_2$Te$_3$ film surface is hydrophilic in

Table 1 The (2θ) angle of diffraction peaks and corresponding crystallites size in La$_2$Te$_3$ thin film deposited on a stainless steel substrate

2θ (degree)	Plane (hkl)	Crystallite size D (nm)
22.59	(211)	38.19
27.27	(220)	67.90
35.02	(321)	27.95
40.60	(110)	31.348
63.21	(541)	125.19
74.48	(642)	48.36

Paper

Table 2 Assignment of functional groups to wavenumbers for the La_2Te_3 material reported by the CBD route, using the FTIR data

Wavenumber (cm^{-1})	Assignment
1012	La(O–H)
1090	(–C–O)
1294	(C–N)
1486	δ(C–H)
1578	υ(C–C)
1670	(La$_2$O$_3$)
1681	La$_2$Te$_3$

Fig. 3 The contact angle image of the La_2Te_3 film surface, where a water droplet is used as the solvent.
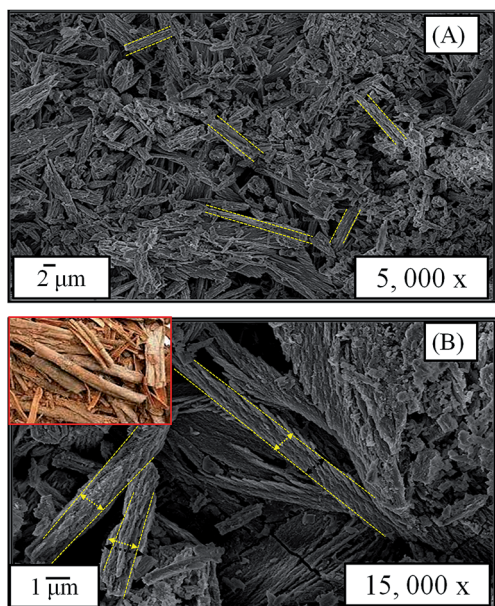

Fig. 2 (A and B) FE-SEM micrographs of La_2Te_3 film with different magnifications showing cinnamon-like microstructure (top inset (B) shows the actual photograph of cinnamon).

nature (a hydrophilic surface exhibits a contact angle less than 90°, and if the contact angle is greater than 90°, then the surface is hydrophobic). As is well known, the material wettability is an intrinsic property for the liquid resting on a solid substrate, resulting from the intermolecular interactions between a liquid and solid.[23] The hydrophilic nature of the La_2Te_3 film surface is useful for the electrolyte to have close contact with the film surface in electrochemical applications. A nanocrystalline material with a hydrophilic nature is one of the prime requirements for the enhancement of electrochemical performance.[24]

Supercapacitive performance

Cyclic voltammetry (CV) study. The cinnamon-like La_2Te_3 exhibits an excellent supercapacitive performance, including a high specific capacitance and excellent rate capability. The capacitance performance of the La_2Te_3 electrode was evaluated using a three-electrode cell configuration in a 1 M KOH electrolyte. The well-known electrochemical redox reaction in which
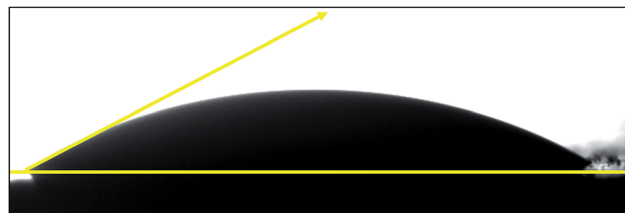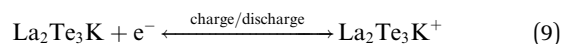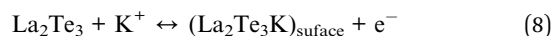
electrons are stored and then released during a redox reaction takes place.[25] In the aqueous KOH electrolyte, K$^+$ plays an important role as assumed in following reactions:

$$La_2Te_3 + K^+ \leftrightarrow (La_2Te_3K)_{suface} + e^- \tag{8}$$

$$La_2Te_3K + e^- \xleftarrow{\text{charge/discharge}} La_2Te_3K^+ \tag{9}$$

The oxidation and reduction process of the La_2Te_3 electrode material in the KOH electrolyte was observed through the ion intercalation and de-intercalation of K$^+$ ions in the La_2Te_3 active material. A well-defined pair of redox peaks between −0.3 and −1.3 V/SCE can be attributed to an excellent redox reaction related to La and Te. The crystal orientation of the cinnamon-like La_2Te_3 suggests that more La sites are exposed to the aqueous electrolyte due to the preferred growth of the (220) plane. The interfacial (C_i) and specific (C_s) capacitances from the CV curves are calculated using the following formulae:

$$C_i = \frac{\int I dt}{dV/dt} \text{ and } C_s = \frac{C_i}{m} \tag{10}$$

where $\int I dt$ is the average current density per unit area, dV/dt is the scan rate, and m is the mass of the active electrode material dipped in the electrolyte.

Effect of the scan rate. The electrochemical performance of La_2Te_3 was tested as a supercapacitive electrode. As shown in Fig. 4(A), the La_2Te_3 electrode was able to function in a wide range of scan rates, ranging from 2 to 100 mV s^{-1} scan rate. It is seen that, there was little change in the oxidation and reduction potentials of the La_2Te_3 electrode material during K$^+$ insertion and extraction at various scan rates. The reduction and oxidation current peaks of La_2Te_3 are clearly visible in the CV curves, and no additional peaks are observed within the potential range. When the scan rate increases, the peak current increases, suggesting that the La_2Te_3 electrode has an excellent rate performance and can result in rapid redox reactions.[26] From Fig. 4(B), the specific capacitance of the cinnamon-like La_2Te_3 electrode was found to be 469 F g^{-1} at a scan rate of 2 mV s^{-1}, which is more than that of other metal chalcogenides such as CoS (363 F g^{-1}),[27] Sm$_2$S$_3$ (294 F g^{-1}),[7] and La$_2$S$_3$ (256 F g^{-1}).[8] At a lower scan rate, a higher surface area can improve the utilization rate of the electrode material during the electrochemical redox process;[28] therefore, greater capacitance values are found at lower scan rates. The specific capacitance decreases as the

scan rate increases, indicating that the cinnamon-like La_2Te_3 electrode shows a good rate capability. The superior performance of the cinnamon-like morphological La_2Te_3 electrode can be ascribed to its porous structure (seen in Fig. 3), which is beneficial for electrolyte penetration and hence facilitates ion diffusion within the La_2Te_3 electrode material.[29]

Galvanostatic charge–discharge (GCD) study

The charge–discharge curves for the cinnamon-like La_2Te_3 electrode at various current densities from 1 to 4 mA cm^{-2} are illustrated in Fig. 4(C). As seen in Fig. 4(C), the discharge curves are not linear in the total potential range at various current densities. It is divided into three different regions. In first region (ΔV_1), there is a sudden drop in the potential (-0.3 to -0.75 V) with time, due to the internal resistance of the La_2Te_3 electrode material.[30] The initial voltage drop indicates that the equivalent series resistance (ESR) is restricted to electron transfer and causes little voltage limitations for the La_2Te_3 electrode. In the second region (ΔV_2), a linear variation of the potential with time is observed, which indicates a double layer capacitance due to the charge separation at the

electrode and electrolyte interface. The third region (ΔV_3) refers to the slope variation of the potential with time, indicating the pseudo-capacitive behavior of the cinnamon-like La_2Te_3 electrode.[31]

The inset of Fig. 4(C) shows an obvious decrease of the capacitance from 455 to 220 F g^{-1} with an increase in the current density from 1 to 4 mA cm^{-2}. The cinnamon-like La_2Te_3 electrode shows higher capacitance values at a low current density due to the faster charge transfer at the interface of the electrode and electrolyte.[32] When the current density increases, the IR drop increases due to the ohmic resistance of the electrode, which blocks the dynamic accommodation of the hydrated ions at the surface of the electrode, resulting in lower capacitance retention at high current density.[33] Moreover, as the charging current density is increased, the charging process of La_2Te_3 is difficult due to the limited migration of K$^+$ ions in the electrode surface, which has a low ionic conductivity.

Ragone plot

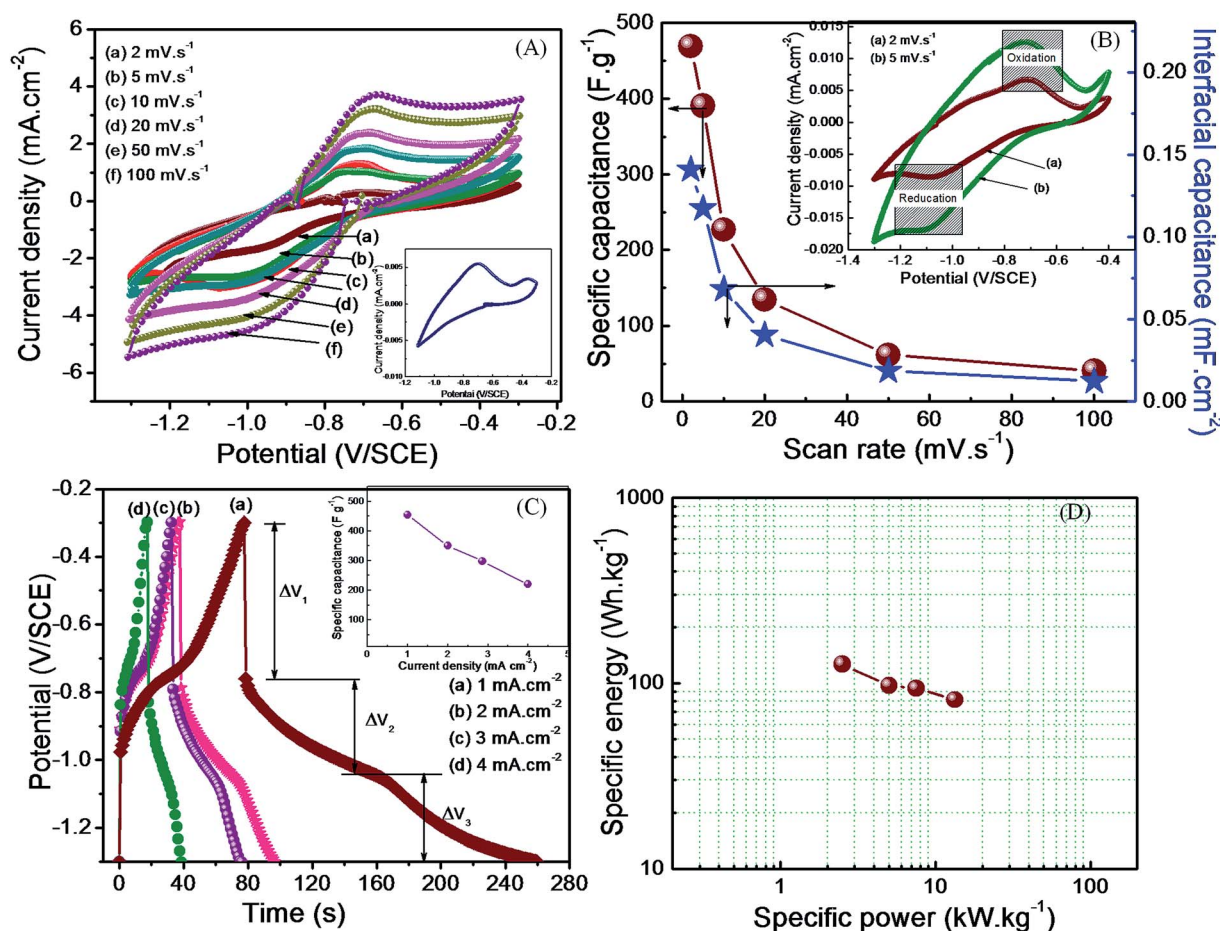The most important parameters, which determine the energy storage capability of the supercapacitor electrode, are the

Fig. 4 (A) Cyclic voltammograms (CVs) of the La_2Te_3 electrode at different scan rates of 2, 5, 10, 20, 50 and 100 mV s^{-1} in a 1 M KOH electrolyte. (B) The graph of the interfacial and specific capacitances for the same scan rate of the La_2Te_3 electrode calculated from the CV curves, inset shows enlarged CV curves for the 2 and 5 mV s^{-1} scan rate. (C) Galvanostatic charge–discharge (GCD) curves (inset show the variation in specific capacitance) with different discharge current densities. (D) Ragone plot of the La_2Te_3 electrode.

Table 3 Parameters of the La_2Te_3 electrode at different current densities obtained from the Ragone plots

Current density (mA cm^{-2})	Specific power (kW kg^{-1})	Specific energy (Wh kg^{-1})	Specific capacitance (F g^{-1})
1	2.5	126.28	455
2	5.0	97.22	350
3	7.5	93.75	337
4	13.33	81.48	214

specific energy and specific power. The Ragone plot (specific energy *versus* specific power) for the La_2Te_3 electrode is plotted in Fig. 4(D) at different current densities. The specific energy of La_2Te_3 electrode decreased from 126 to 81 Wh kg^{-1} with increase in current density (1 to 4 mA cm^{-2}) as shown in Table 3. The La_2Te_3 electrode exhibits a maximum specific energy of ~126 Wh kg^{-1} at a specific power of 2.5 kW kg^{-1}, which provides a comparatively high specific energy in relation to an La_2S_3 electrode.[8] An excellent performance of an La_2S_3 electrode is expected to provide an ultra high specific energy or high specific capacitance at high charge–discharge rates.

Cyclic stability study

Cyclic stability is one of the most important part in the performance of a supercapacitor electrode. Fig. 5(A) reveals the electrochemical cyclic performance of the La_2Te_3 electrode recorded over 1000th cycles with a 50 mV s^{-1} scan rate. Fig. 5(B) illustrates the change in the specific capacitance of the La_2Te_3

electrode with the cycle number. The specific capacitance decreases from 63 to 45 F g^{-1} with a 71% capacity retention over 1000 cycles. Zhu *et al.*[34] showed about 74% of stability for a nickel sulfide electrode over 1000 cycles in a KOH electrolyte, which is nearly same as the cinnamon-like La_2Te_3 electrode. The decay observed in the cycling stability may be due to the dissolution of the electrode active material in the electrolyte and capacity imbalances between the electrodes, which causes the instability of the electrode potential.[35] Therefore, the La_2Te_3 electrode exhibits good stability in the −0.3 to −1.3 V/SCE window range.

Electrochemical impedance spectroscopy (EIS) study

EIS is a powerful technique to understand the fundamental behavior of an electrode material in an electrolyte. The EIS measurements were performed at room temperature to obtain information on the electrode material surface, charge-transfer resistance and phase angle. The impedance data are analyzed
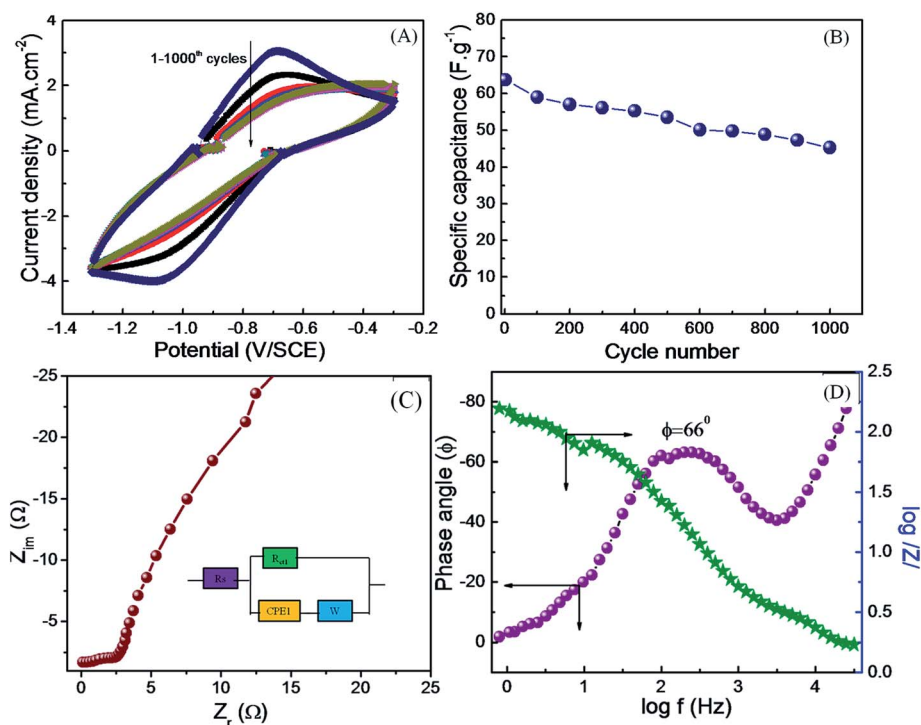

Fig. 5 (A) The electrochemical CV curves, (B) capacitive retention *versus* cycle number for the La_2Te_3 electrode recorded over 1000th cycles at a 50 mV s^{-1} scan rate. (C) Nyquist plot, (inset shows the equivalent circuit for the best-fitted impedance data) and (D) Bode plot of phase angle and log |z| *versus* frequency of the La_2Te_3 electrode recorded in 1 kHz to 0.1 Hz frequency range.

using a Nyquist plot, which shows the frequency response of the La_2Te_3 electrode. A Nyquist plot is the plot of the imaginary component (Z'') of the impedance against the real component (Z') in the frequency range of 1 MHz to 0.1 Hz, as shown in Fig. 5(D).

The Nyquist plot shows a small semicircle at higher frequency regions, which can be attributed to the charge transfer process. The equivalent series resistance (ESR) can be obtained at the mid frequency region from the X-intercept of the Nyquist plots, and the ESR of the La_2Te_3 electrode was 3.2 Ω. At the low frequency range, the straight line is attributed to the ion diffusion in the electrolyte, which is called the Warburg impedance. If the Warburg angle is higher than 45° in the low frequency region, then it indicates that the electrode is strongly controlled by an ion diffusion process.[36] All of these results indicated that the La_2Te_3 material is a suitable electrode for a supercapacitor device. In the inset of the Nyquist plot, the equivalent circuit shows the best fitted impedance data of the La_2Te_3 electrode. From the circuit diagram, it is observed that, R_s corresponds to the resistance of the electrolyte (0.3 Ω) independent of the frequency, R_{ct} is the charge transfer resistance (2.9 Ω), CPE is the non-ideal EDLC and W represents the diffusion Warburg impedance ($W = 0.02$).

Bode plot

Fig. 5(D) illustrates the Bode plot of the La_2Te_3 electrode. From the graph, the frequency (f_0) corresponds to peak value of Z_{im} within the high frequency region, which is even comparable to the values for supercapacitors with aqueous electrolytes. Thus, the relaxation time constant, τ_0 was calculated to be about 0.5 s by the equation, $\tau_0 = 1/f_0$. The phase angle of the La_2Te_3 electrode was about 66° at a frequency of 0.1 Hz with a shallower slope due to the pseudocapacitive behavior. The cinnamon-like La_2Te_3 leads to a low electrolyte resistance and makes the K^+ ions deintercalate and intercalate very easily because of the very short diffusion distance.

Device fabrication and performance evaluation of a portable La_2Te_3 asymmetric aqueous supercapacitor device

Device fabrication

To evaluate the supercapacitive performance of a portable La_2Te_3/graphite electrode in aqueous electrolyte, a cinnamon-like La_2Te_3 based asymmetric supercapacitor device was fabricated. The schematic diagram concerning the fabrication of the asymmetric aqueous supercapacitor device based on the La_2Te_3 electrode (2×3 cm^2) is illustrated in Fig. 6(A–D). The schematic consists of a portable La_2Te_3 thin film as the working electrode assembled in a cylindrical plastic jacket. A graphite electrode was inserted at the centre of the assembly without any contact to the working La_2Te_3 electrode. The assembly was filled with 1 M KOH electrolyte with a mass loading of the La_2Te_3 electrode of 0.1 mg cm^{-2}. The supercapacitive performance of the portable asymmetric supercapacitor device based on the La_2Te_3 electrode was tested by means of CV, GCD and impedance studies.

Performance evaluation of the portable La_2Te_3 asymmetric supercapacitor device

Fig. 7(A) demonstrates the typical cyclic voltammogram (CV) curves of the portable La_2Te_3 asymmetric supercapacitor device recorded at a scan rate ranging from 5 to 100 mV s^{-1} in the potential between −0.3 and −1.3 V. From the CV curves, the maximum specific capacitance of the device was calculated to be 19.5 F g^{-1} at a low scan rate of 5 mV s^{-1}, as seen in Fig. 7(B). There was no significant change in shape of the CV curves by the increase in scan rate. This indicates the improved mass transportation and electron conduction within the La_2Te_3 asymmetric electrode.[37] Fig. 7(C) shows the GCD curves of the portable La_2Te_3 asymmetric supercapacitor device with different current densities and the inset displays the graph of
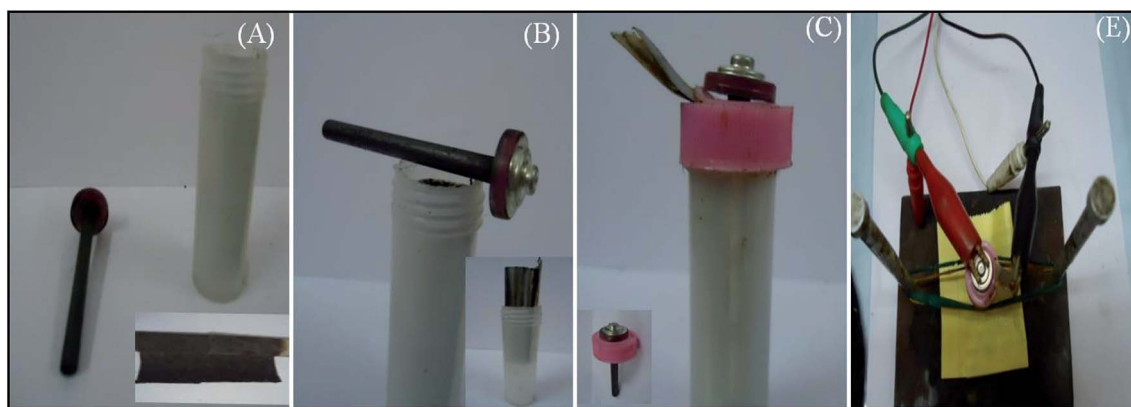

Fig. 6 Digital photographs of the fabrication process of a portable graphite/La_2Te_3 asymmetric supercapacitor device, (A) graphite, portable La_2Te_3 electrode and plastic jacket ready for device fabrication, (B) rolled portable La_2Te_3 electrode and insertion into plastic jacket, (C) actual fabricated asymmetric supercapacitor device, and (D) La_2Te_3/graphite asymmetric supercapacitor device connected to a battery cycler for performance evaluation.
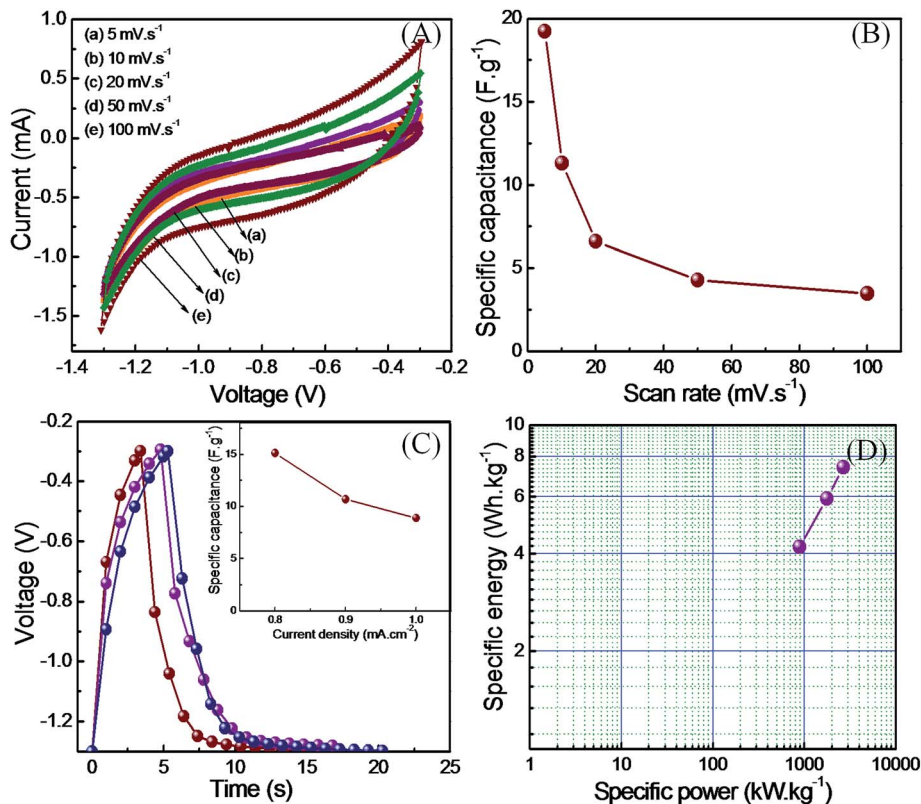
Fig. 7 (A) Cyclic voltammogram (CV) curves and (B) specific capacitance values recorded for portable La_2Te_3 asymmetric supercapacitor device at different scan rates in 1 M KOH electrolyte. (C) GCD curves at 0.8, 0.9 and 1 mA cm^{-2} current densities and inset shows the corresponding capacitance values, and (D) Ragone plot of the La_2Te_3 asymmetric supercapacitor device derived from the discharging curves.
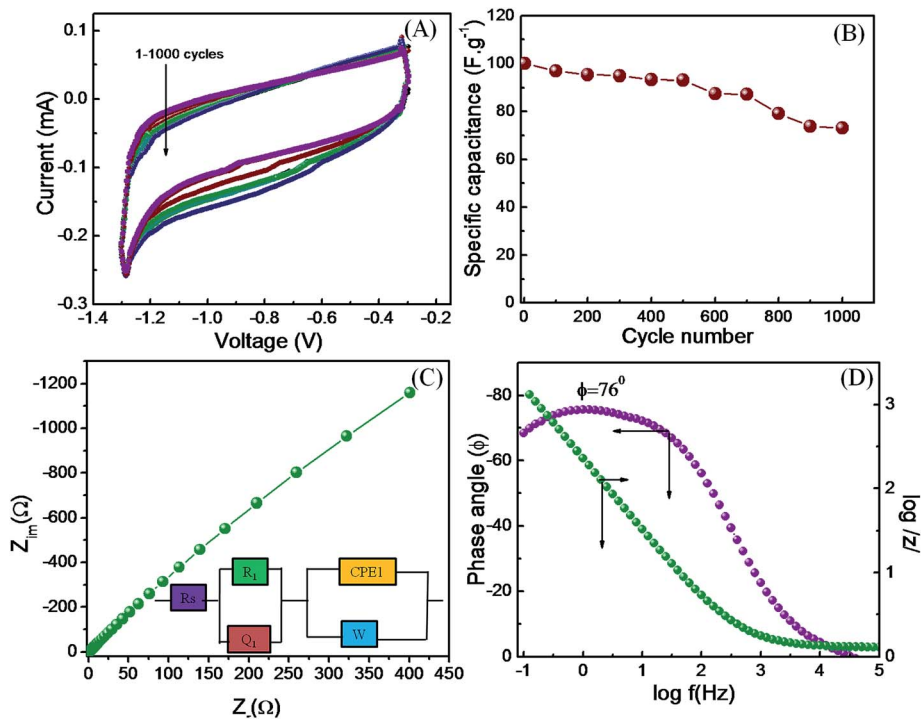

Fig. 8 (A) The electrochemical cyclic stability studies and (B) Specific capacitance as a function of cycle numbers of the portable La_2Te_3 asymmetric supercapacitor device at 50 mV s^{-1} scan rate over 1000th cycles. (C) Nyquist plot, and (D) Bode plot of the portable La_2Te_3 asymmetric supercapacitor device.

the corresponding specific capacitances *versus* current densities. It is observed that, the specific capacitance slightly decreases with increase in the charging current density. The obtained values of the specific capacitances from the discharge profile are in good agreement with those calculated from the CV curve. Fig. 7(D) is the Ragone plot of the portable La_2Te_3 asymmetric supercapacitor device, which reveals the specific energy of 4, 6, 7.4 Wh kg^{-1} with specific power as 888, 1777 and 2666 W kg^{-1} at the current densities of 0.8, 0.9 and 1 mA cm^{-2}, respectively. At the higher current density, the capacitance was found to be 15 F g^{-1}, which indicates that the supercapacitive properties of the portable La_2Te_3 asymmetric supercapacitor device are better.

The cyclic stability of the portable La_2Te_3 asymmetric supercapacitor device was evaluated through cyclic voltammetry. Fig. 8(A) exhibits the CV curves recorded at a 50 mV s^{-1} scan rate over 1000 cycles. The corresponding specific capacitance value as a function of the cycle numbers is shown in Fig. 8(B). The 27% specific capacitance drop observed after 1000 cycles is better than the MoS_2/Graphene electrode reported by Liu *et al.*[38] The Nyquist plot of the portable La_2Te_3 asymmetric supercapacitor device is presented in Fig. 8(C) and the inset shows the equivalent circuit with the best fitted impedance data. The obtained impedance spectrum of the supercapacitor device shows an electrolyte resistance of 0.09 Ω. In mid-high frequency region, the charge transfer resistance was found to be 0.3 Ω (R_{ct}). An inclined line in the low frequency range, which was considered as the Warburg constant (W) of 0.04, was associated with the diffusion of the K^+ ions into the La_2Te_3 electrode material. The much shorter electronic resistance of the asymmetric graphite/La_2Te_3 supercapacitor device compared to the La_2Te_3 electrode shows fast ion diffusion and indicates an EDLC behavior.[39] An asymmetric supercapacitor based on a graphite electrode reduces the contact resistance with an increased charge transfer rate ($\tau_0 = 0.31$ s) and results in the enhancement of the electrochemical redox activities.[40] Huang *et al.*[41] demonstrated a good strategy to fabricate graphene-based electrode materials for supercapacitor applications, which could have lower resistance values in an aqueous KOH electrolyte. The Bode plot shown in Fig 8(D) is the graph of the phase angle (Φ) or log |z| *versus* log f (Hz). The lifetime (τ_0) of electrons in the La_2Te_3 supercapacitor device is inversely proportional to the peak frequency in the Bode phase plot. The increased phase angle to 10° ($\Phi = 76°$) of the asymmetric supercapacitor device is influenced by fast ion diffusion at the interface of the electrode and electrolyte.

Conclusions

La_2Te_3 thin films were successfully synthesized by a chemical bath deposition route. This strategy promotes a new interface design for the cinnamon-like architecture for supercapacitive charge storage devices. The nanostructured La_2Te_3 electrode showed a maximum specific capacitance of 469 F g^{-1} with an excellent charge–discharge response. The La_2Te_3 electrode achieved a high specific capacitance with an ultra high specific

energy. We demonstrate an optimal interface design for the fabrication of La_2Te_3 based asymmetric supercapacitor devices with a high-performance energy conversion and a storage device.

Acknowledgements

References

1 C. D. Lokhande, D. P. Dubal and O.-S. Joo, *Curr. Appl. Phys.*, 2011, **11**, 255.

2 B. Kim, H. Chung and W. Kim, *Nanotechnology*, 2012, **23**, 155401.

3 D. P. Dubal, D. S. Dhawale, R. R. Salunkhe and C. D. Lokhande, *J. Electroanal. Chem.*, 2010, **647**, 60.

4 M. Sasidharan, N. Gunawardhana, S. Chenrayan and M. Yoshioa, *J. Mater. Chem. A*, 2014, **2**, 7337.

5 D. Aradilla, F. Estrany and C. Aleman, *J. Phys. Chem. C*, 2011, **115**, 8430.

6 Z. Stevic and M. Rajcic-Vujasinovic, *J. Power Sources*, 2006, **160**, 1511.

7 V. S. Kumbhar, A. D. Jagadale and C. D. Lokhande, *J. Power Sources*, 2013, **234**, 107.

8 S. J. Patil, V. S. Kumbhar, B. H. Patil, R. N. Bulakhe and C. D. Lokhande, *J. Alloys Compd.*, 2014, **611**, 191.

9 C. Graf, A. Assoud, O. Mayasree and H. Kleinke, *Molecules*, 2009, **14**, 3115.

10 A. F. May, J. P. Fleurial and G. J. Snyder, *Phys. Rev. B: Condens. Matter Mater. Phys.*, 2008, **78**, 125205.

11 M. M. Blanca, I. K. Boris, M. J. Victor, E. M. Perla and T. L. Susana, *Ind. Eng. Chem. Res.*, 2011, **50**, 7705.

12 G. D. Bagde, S. D. Sartale and C. D. Lokhande, *Mater. Chem. Phys.*, 2005, **89**, 402.

13 M. C. Pereira and R. A. Carvalho, *Thermochim. Acta*, 1986, **102**, 311.

14 T. H. Ramsey, H. Steinfink and E. J. Weiss, *J. Appl. Phys.*, 1963, **34**, 2917.

15 A. K. Samal and T. Pradeep, *J. Phys. Chem. C*, 2010, **114**, 5871.

16 A. F. May, Ph D Thesis, High-Temperature Transport in Lanthanum Telluride and Other Modern Thermoelectric Materials, California Institute of Technology Pasadena, California, 2010.

17 O. Skhouni, A. E. Manouni, M. Mollar, R. Schrebler and B. Mari, *Thin Solid Films*, 2014, **564**, 195.

18 J. Kwon, M. Dai, M. D. Halls, E. Langereis, Y. J. Chabal and R. G. Gordon, *J. Phys. Chem. C*, 2009, **113**, 654.

19 B. Stuart, *Infrared spectroscopy: fundamentals and applications*, Wiley-VCH Verlag Gmbh and Co. KGaA, Weinheim, Germany, 2004.

20 V. Mathew, S. Jacob, L. Xavier1 and K. E. Abraham, *J. Rare Earths*, 2012, **30**, 245.

21 M. Malinowskia, W. Lewandowski, R. Swisłocka and E. Regulska, *Spectroscopy*, 2010, **24**, 277.

22 B. H. Patil, G. S. Gund and C. D. Lokhande, *Ionics*, 2014, DOI: 10.1007/s11581-014-1146-8.

23 Z. Bo, W. Zhu, X. Tu, Y. Yang, S. Mao, Y. He, J. Chen, J. Yan and K. Cen, *J. Phys. Chem. C*, 2014, **118**, 13493.

24 P. M. Kulal, D. P. Dubal, C. D. Lokhande and V. J. Fulari, *J. Alloys Compd.*, 2011, **509**, 2567.

25 F. Tao, Y. Q. Zhao, G. Q. Zhang and H. L. Li, *Electrochem. Commun.*, 2007, **9**, 1282.

26 W. Wei, L. Mi, Y. Gao, Z. Zheng, W. Chen and X. Guan, *Chem. Mater.*, 2014, **26**, 3418.

27 P. Justin and G. R. Rao, *Int. J. Hydrogen Energy*, 2010, **35**, 9709.

28 D. Shu, C. Lv, F. Cheng, C. He, K. Yang, J. Nan and L. Long, *Int. J. Electrochem. Sci.*, 2013, **8**, 1209.

29 W. Zhou, K. Zhou, X. Liu, R. Hu and H. Liu, *J. Mater. Chem. A*, 2014, **20**, 7250.

30 A. N. Naveen and S. Selladurai, *Electrochim. Acta*, 2014, **125**, 404.

31 D. P. Dubal and R. Holze, *J. Power Sources*, 2013, **238**, 274.

32 S. N. Pusawale, P. R. Deshmukh, J. L. Gunjakar and C. D. Lokhande, *Mater. Chem. Phys.*, 2013, **139**, 416.

33 A. Vu, X. Li, J. Phillips, A. Han, W. H. Smyrl, P. Buhlmann and A. Stein, *Chem. Mater.*, 2013, **25**, 4137.

34 T. Zhu, Z. Wang, S. Ding, J. S. Chen and X. W. Lou, *RSC Adv.*, 2011, **1**, 397.

35 D. P. Dubal, G. S. Gund, C. D. Lokhande and R. Holze, *Energy Technol.*, 2014, **4**, 401.

36 I. M. Salas, Y. N. Sudhakar and M. Selvakumar, *Appl. Surf. Sci.*, 2014, **296**, 195.

37 X. Meng, M. Zhou, X. Li, J. Yao, F. Liu, H. He, P. Xiao and Y. Zhang, *Electrochim. Acta*, 2013, **109**, 20.

38 Y. Liu, Y. Zhao, L. Jiao and J. Chen, *J. Mater. Chem. A*, 2014, **2**, 13109.

39 S. Ye and J. Feng, *ACS Appl. Mater. Interfaces*, 2014, **6**, 9671.

40 G. Huang, T. Chen, Z. Wang, K. Chang and W. Chen, *J. Power Sources*, 2013, **235**, 122.

41 M. L. Huang, C. D. Gu, X. Ge, X. L. Wang and J. P. Tu, *J. Power Sources*, 2014, **259**, 98.